Mathematical Modeling of Transport Phenomena in Polymer Electrolyte and Direct Methanol Fuel Cells

ERIK BIRGERSSON



KTH Mechanics

Doctoral Thesis Stockholm, Sweden 2004

Mathematical Modeling of Transport Phenomena in Polymer Electrolyte and Direct Methanol Fuel Cells

by

Erik Birgersson

February 2004
Technical Reports from
Royal Institute of Technology
Department of Mechanics
S-100 44 Stockholm, Sweden

Typsatt i $\mathcal{A}_{\mathcal{M}}\mathcal{S}$ - $\mathbb{A}_{T_{\mathbf{E}}}X$.

Akademisk avhandling som med tillstånd av Kungliga Tekniska Högskolan i Stockholm framlägges till offentlig granskning för avläggande av teknologie doktorsexamen den 4 Februari 2004 kl 10.15 i Kollegiesalen, Administrationsbyggnaden, Kungliga Tekniska Högskolan, Valhallavägen 79, Stockholm.

©Erik Birgersson 2004 Universitetsservice US-AB, Stockholm 2004

Mathematical Modeling of Transport Phenomena in Polymer Electrolyte and Direct Methanol Fuel Cells

Erik Birgersson

Department of Mechanics, Royal Institute of Technology SE-100 44 Stockholm, Sweden.

Abstract

This thesis deals with modeling of two types of fuel cells: the polymer electrolyte fuel cell (PEFC) and the direct methanol fuel cell (DMFC), for which we address four major issues: a) mass transport limitations; b) water management (PEFC); c) gas management (DMFC); d) thermal management.

Four models have been derived and studied for the PEFC, focusing on the cathode. The first exploits the slenderness of the cathode for a two-dimensional geometry, leading to a reduced model, where several nondimensional parameters capture the behavior of the cathode. The model was extended to three dimensions, where four different flow distributors were studied for the cathode. A quantitative comparison shows that the interdigitated channels can sustain the highest current densities. These two models, comprising isothermal gasphase flow, limit the studies to (a). Returning to a two-dimensional geometry of the PEFC, the liquid phase was introduced via a separate flow model approach for the cathode. In addition to conservation of mass, momentum and species, the model was extended to consider simultaneous charge and heat transfer for the whole cell. Different thermal, flow fields, and hydrodynamic conditions were studied, addressing (a), (b) and (d). A scale analysis allowed for predictions of the cell performance prior to any computations. Good agreement between experiments with a segmented cell and the model was obtained.

A liquid-phase model, comprising conservation of mass, momentum and species, was derived and analyzed for the anode of the DMFC. The impact of hydrodynamic, electrochemical and geometrical features on the fuel cell performance were studied, mainly focusing on (a). The slenderness of the anode allows the use of a narrow-gap approximation, leading to a reduced model, with benefits such as reduced computational cost and understanding of the physical trends prior to any numerical computations. Adding the gas-phase via a multiphase mixture approach, the gas management (c) could also be studied. Experiments with a cell, equipped with a transparent end plate, allowed for visualization of the flow in the anode, as well as validation of the two-phase model. Good agreement between experiments and the model was achieved.

Descriptors: Fuel cell; DMFC; PEFC; one-phase; two-phase; model; visual cell; segmented cell; scale analysis; asymptotic analysis.

Preface

This thesis considers modelling of transport phenomena in polymer electrolyte and direct methanol fuel cells. The thesis is based on the following papers:

- Paper 1. Vynnycky, M. and Birgersson, E. 2002, 'Analysis of a Model For Multicomponent Mass Transfer in the Cathode of a Polymer Electrolyte Fuel Cell'. SIAM (Soc. Ind. Appl. Math.) Journal of Applied Mathematics, 63, 1392-1423 (2003).
- **Paper 2.** Birgersson, E. and Vynnycky, M. 2002, 'A Quantitative Study of the Effect of Flow-Distributor Geometry in the Cathode of a PEFC'. *Manuscript*.
- **Paper 3.** Birgersson, E., Noponen, M., and Vynnycky, M., 'Analysis of a Two-phase Non-Isothermal Model for a PEFC'. *Manuscript*.
- **Paper 4.** Noponen, M., Birgersson, E., Ihonen, J., Vynnycky, M., Lundblad, A. and Lindbergh, G., 'A Two-Phase Non-Isothermal PEFC Model: Theory and Validation'. Submitted to Fuel Cells From Fundamentals to Systems (2003).
- **Paper 5.** Birgersson, E., Nordlund, J., Ekström, H., Vynnycky, M. and Lindbergh, G., 'Reduced Two-Dimensional One-Phase Model for Analysis of the Anode of a DMFC'. *Journal of the Electrochemical Society*, **150**, A1368-A1376 (2003).
- **Paper 6.** Nordlund, J., Picard, C., Birgersson, E., Vynnycky, M. and Lindbergh, G., 'The Design and Usage of a Visual Direct Methanol Fuel Cell'. Submitted to Journal of Applied Electrochemistry (2003).
- **Paper 7.** Birgersson, E., Nordlund, J., Vynnycky, M., Picard, C. and Lindbergh, G., 'Reduced Two-Phase Model for Analysis of the Anode of a DMFC'. *To be submitted to Journal of the Electrochemical Society.*

The papers are re-set in the present thesis format.

PREFACE

Division of work between authors

- **Paper 1:** The problem formulation was performed jointly by the authors. The analysis, coding and numerical simulations were performed by M. Vynnycky (MV). Post-processing of data was performed by MV and E. Birgersson (EB). The report was written mainly by MV, with feedback from EB.
- **Paper 2:** The problem formulation, coding, numerical simulations and post-processing were performed by EB. The report was written mainly by EB, with feedback from MV.
- **Paper 3:** The problem formulation for the mathematical model, coding, numerical simulations and post-processing were performed in close cooperation between M. Noponen (MN) and EB. EB performed the analysis with feedback from MV. The report was written by EB and MN, with feedback from MV.
- **Paper 4:** The problem formulation for the mathematical model, coding, numerical simulations and post-processing were performed in close cooperation between MN and EB. The experiments were carried out by MN and J. Ihonen (JI). The report was written by EB and MN, with feedback from MV.
- Paper 5: The problem formulation, analysis, coding, numerical simulations and post-processing were performed by EB with feedback from MV. J. Nordlund (JN) provided the electrokinetics and the main part of the constitutive relations and parameters. The report was written in close cooperation between EB and JN, with feedback from MV and G. Lindbergh (GL).
- **Paper 6:** The problem formulation was performed mainly by JN, with some feedback from EB. The cell was designed by JN and the peripheral equipment set up by JN and Cyril Picard (CP). The experiments and post-processing were carried out by CP under supervision of JN for the electrochemical part and EB for the hydrodynamic part. The report was written by JN, with feedback from EB, CP, GL and MV.
- Paper 7: The problem formulation, analysis and coding were performed by EB with feedback from MV. JN provided the electrokinetics, equilibrium conditions and the main part of the constitutive relations and parameters. The experiments were carried out by CP under supervision of JN for the electrochemical part and EB for the hydrodynamic part. Numerical simulations and post-processing were performed by EB and JN. The report was written in close cooperation between EB and JN, with feedback from MV.

Contents

 iv

8

Preface

Chapter 1. Introduction

Chapter 2. Fuel cells	10
1. Basic principles	10
2. Overview of fuel cell technologies	12
3. Polymer electrolyte and direct methanol fuel cells	13
Chapter 3. Basic concepts	17
1. Volume averaging	17
2. Governing equations	18
3. Electrokinetics and the active layers	23
4. Scale analysis and nondimensional numbers	25
5. Numerical tools and methodologies	27
Chapter 4. Summary of results	28
1. Polymer electrolyte fuel cells	28
2. Direct methanol fuel cells	33
Chapter 5. Discussion and Outlook	38
Acknowledgments	40
Bibliography	41
Paper 1: Analysis of a Model For Multicomponent Mass Transfer in the Cathode of a Polymer Electrolyte Fuel Cell	
Paper 2: A Quantitative Study of the Effect of Flow-Distributor Geometry in the Cathode of a PEM Fuel Cell	
Paper 3: Analysis of a Two-phase Non-Isothermal Model for a PEFC	
Paper 4: A Two-Phase Non-Isothermal PEFC Model: Theory and Validation	
Paper 5: Reduced Two-Dimensional One-Phase Model for Analysis of the Anode of a DMFC	

CONTENTS vii

Paper 6: The Design and Usage of a Visual Direct Methanol Fuel Cell

Paper 7: Reduced Two-Phase Model for Analysis of the Anode of a DMFC

CHAPTER 1

Introduction

In view of ever increasing levels of environmental pollution and thus a desire to replace the fossil-fuel-based economy with a cleaner alternative, the fuel cell has in recent years emerged as a prime candidate for automotive, portable and stationary applications. These fuel cells convert hydrogen or hydrocarbon fuels directly into electricity. High efficiency, as the fuel cell is not limited by the Carnot-efficiency, low emissions, silent operation, no moving parts and a scalable system, number among the main advantages of fuel cells.

At present, however, despite vast amounts of capital dedicated to R&D, only a few commercial applications can be found, as the production cost remains too high to contend with traditional power sources, such as batteries and combustion engines, without significant market drivers. In addition to reducing the cost by developing new materials and improved construction techniques, the fuel issue has to be solved satisfactorily: either by fuel storage of pure hydrogen or by reforming of hydrocarbon fuels. Reductions in cost and advancement of the fuel cell technology are still feasible, though hindered by the highly interdisciplinary nature of fuel cells systems, which is one of the reasons why commercialisation of the fuel cell, despite its effect being discovered as early as 1838 by Christian Friedrich Schönbein¹ [1], is still in its cradle. Thus, although the first operating fuel cell was constructed by Sir William Robert Grove in 1839, a drawing of which is shown in Figure 1.1, it would take more than a century, until the 1990s, for fuel cell activities to mushroom around the world.

This thesis addresses two types of fuel cells, namely the polymer electrolyte fuel cell² (PEFC) and its sibling, the direct methanol fuel cell (DMFC), with the aim to further the development of mathematical models for these. Such models are necessary for understanding the inherent transport processes that occur in a fuel cell, for improving the design and materials, as well as allowing for fast studies of fuel cell systems. The difficulty in modelling a fuel cell stems from the variety of engineering disciplines, ranging from material science over electrochemistry to fluid dynamics that have to be considered. A model, incorporating all of the relevant physics of the various components in a fuel cell, would be three-dimensional, non-isothermal, multicomponent and

¹Contrary to common belief, it was C. F. Schönbein who discovered the fuel cell effect and not W. R. Grove [1].

²Also commonly referred to as proton exchange membrane fuel cell (PEMFC) or solid polymer fuel cell (SPFC).

multiphase. In addition, the model should take into account charge transfer, change of phase, electroosmosis, electrochemical reactions, and dynamic behavior, resulting in a highly complicated model that would easily lose tractability. Therefore, the complexity of a fuel cell is usually reduced by focusing on some aspects of the phenomena occurring. In this thesis, we focus our attention on the cathode of the PEFC and the anode of the DMFC: the cathode of the PEFC is more limiting due to its sluggish kinetics, as compared to the fast hydrogen oxidation at the anode, provided that the hydrogen feed stream is sufficiently pure to avoid poisoning of the catalyst and sufficiently hydrated; the anode of the DMFC, however, is of interest due to its complex reaction kinetics.

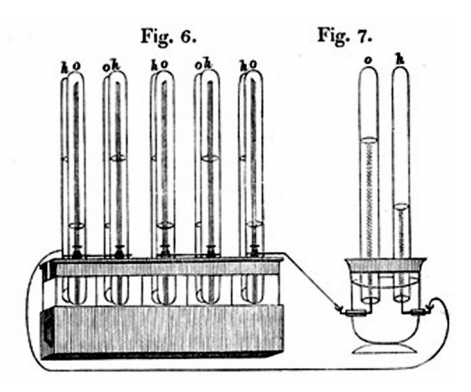


Figure 1.1. Grove's drawing of one of his experimental "gas batteries", later renamed as the fuel cell, from a letter dated 1843. The gas battery comprises 5 tubes (Fig. 6), filled with oxygen (o) and hydrogen (h). A voltmeter (Fig. 7) is connected to the "gas battery". Courtesy of the Smithsonian Institute.

In chapter two, the workings of a fuel cell in conjunction with an overview of the fuel cell technologies of today are introduced, with special attention given the aforementioned fuel cells: PEFC and DMFC. The following chapter summarizes the basic concepts for modelling, i.e. volume averaged quantities, governing equations, inherent electrochemistry in the active layers, scale analysis with nondimensional numbers and finishes with the main numerical tools and methodologies. Chapter four provides a summary of the papers that form the basis of this thesis and in the last chapter, the main results are discussed and an outlook for possible extensions in terms of experiments and mathematical modelling is given. At the end of the thesis, the papers can be found.

CHAPTER 2

Fuel cells

In this chapter, the basic principles of a fuel cell are introduced, comprising the inner workings as well as an overview of available fuel cell technologies. As was mentioned in the introduction, we will focus on the polymer electrolyte and direct methanol fuel cell, of which more details will be given, especially in terms of already existing mathematical models.

1. Basic principles

A fuel cell is an electrochemical device that directly converts chemical energy into electric energy, and thus is not limited by the Carnot efficiency.

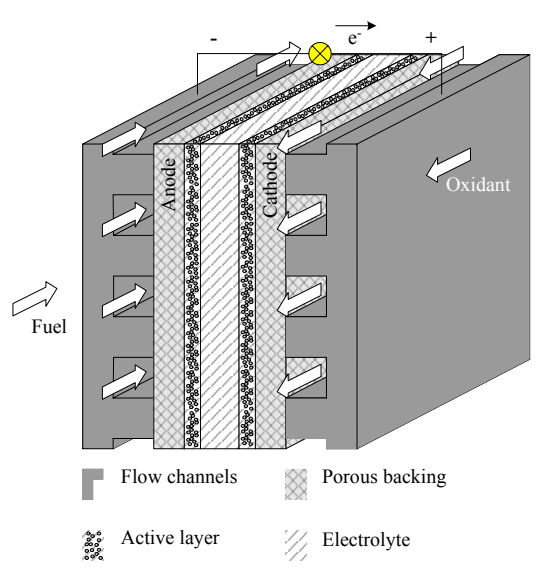


Figure 2.1. A schematic of a fuel cell.

Fuel cells differ from primary and secondary batteries in how the fuel and oxidant are stored: a primary battery is useless once the stored fuel/oxidant is depleted; a secondary battery can be recharged, allowing for several recharges; in the fuel cell, the fuel and oxidant are fed continuously and as such does not require any recharging. A schematic of a fuel cell is depicted in Figure 2.1.

The basic cell consists of two porous electrodes³, termed the anode and the cathode, separated by an electrolyte. These three components constitute the heart of the fuel cell, also referred to as membrane electrode assembly⁴ (MEA), sandwiched between two porous backings⁵ and flow distributors. The flow distributors usually comprise flow channels machined into a bipolar plate, as illustrated in Figure 2.1, or net-type flow fields. In the course of operation, an oxidant is fed at the inlet on the cathode side and transported to the electrolyte/cathode interface; the fuel on the other hand, is fed at the anode inlet and is transported to the electrolyte/anode interface. The reactions at the electrodes are kept separated by the electrolyte, with electrons that can drive a load through an external circuit, flowing from the anode to the cathode and ions passing through the electrolyte to close the electric circuit.

The performance of a fuel cell is usually given by a polarization curve, where the cell voltage is related to the current density, or by a power density curve, where the power density is given as a function of the current density of the cell, as illustrated in Figure 2.2.

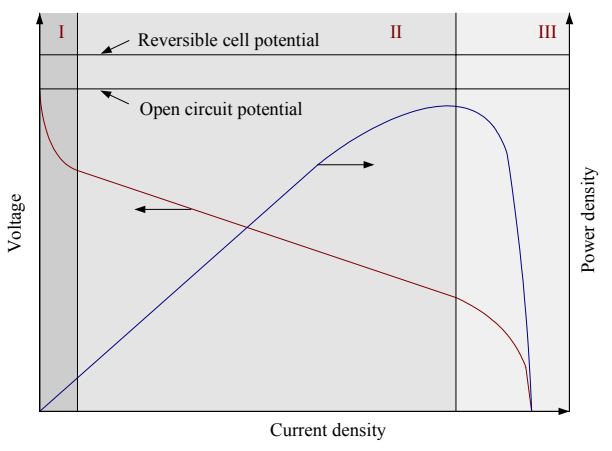


Figure 2.2. A schematic of a polarization curve and power density curve.

The polarization curve approaches the open circuit potential as the current decreases and not the reversible cell potential as might be expected, when no current is drawn from the cell. This loss in voltage can be attributed to fuel crossover and internal currents. In Figure 2.2, three regions can be discerned: region I, where the rapid non-linear drop in voltage originates from activation losses; region II, where the voltage loss is more linear, stemming from ohmic losses, such as bulk and interface resistances; region III, where the voltage falls

³Also known as active layers.

 $^{^4\}mathrm{The}$ MEA is not clearly defined and can sometimes include the porous backings.

⁵These porous layers are sometimes referred to as "gas diffusion layers", which is misleading, since the transport of mass and species is by no means limited to just diffusion and the gas phase.

swiftly due to mass transport limitations in the cell. The optimal operating regime for a fuel cell is up to the maximum of the power density to avoid the sharp decrease in power density that occurs in region III.

2. Overview of fuel cell technologies

The existing fuel cell types can be classified according to the type of electrolyte, operating temperature or fuel/oxidant used. According to [2], there are five types of fuel cells that are viable today; we will add a sixth, namely the direct methanol fuel cell, to this list:

- (1) Polymer electrolyte fuel cell (PEFC): The PEFC operates at low temperatures, $\sim 20-90^{\circ}\text{C}$, and is equipped with a solid polymer electrolyte. Vehicles, low power CHP⁶ systems and mobile application are feasible.
- (2) Direct methanol fuel cell (DMFC): The DMFC operates at low temperatures, $\sim 20-110^{\circ}$ C, and is similar to the PEFC equipped with a solid polymer electrolyte. Potential and present applications include portable devices.
- (3) Alkaline Fuel Cell (AFC): The AFC operates at low temperatures, $\sim 60-220^{\circ}\text{C}$, with a liquid electrolyte, comprising OH⁻. This type of fuel cell was used on the Apollo craft.
- (4) Phosphoric acid fuel cell (PAFC): The PAFC operates at medium temperatures, $\sim 150-220^{\circ}\mathrm{C}$, with a liquid electrolyte, comprising concentrated phosphoric acid. This type of fuel cell was the first to be commercialized. It is well suited for medium scale CHP systems, such as office buildings and schools.
- (5) Molten carbonate fuel cell (MCFC): The MCFC operates at high temperatures, $\sim 650^{\circ}$ C, with an electrolyte, comprising molten carbonate. Present and potential applications are for medium to large scale CHP systems.
- (6) Solid oxide fuel cell (SOFC): The SOFC operates at high temperatures, $\sim 500-1000^{\rm o}$ C, with an electrolyte, comprising a ceramic oxygen conductor. Suitable for all CHP systems.

A more detailed description of these fuel cells can be found in e.g. [2].

⁶Combined heat and power.

3. Polymer electrolyte and direct methanol fuel cells

Out of the six aforementioned fuel cells, we will focus on the two closely related fuel cells PEFC and DMFC. The main difference between the two is the fuel on the anode side: hydrogen for the former and methanol for the latter. A schematic of a cross-section in the normal and spanwise direction for these is shown in Figure 2.3 (the streamwise direction is given by the arrows in Figure 2.1).

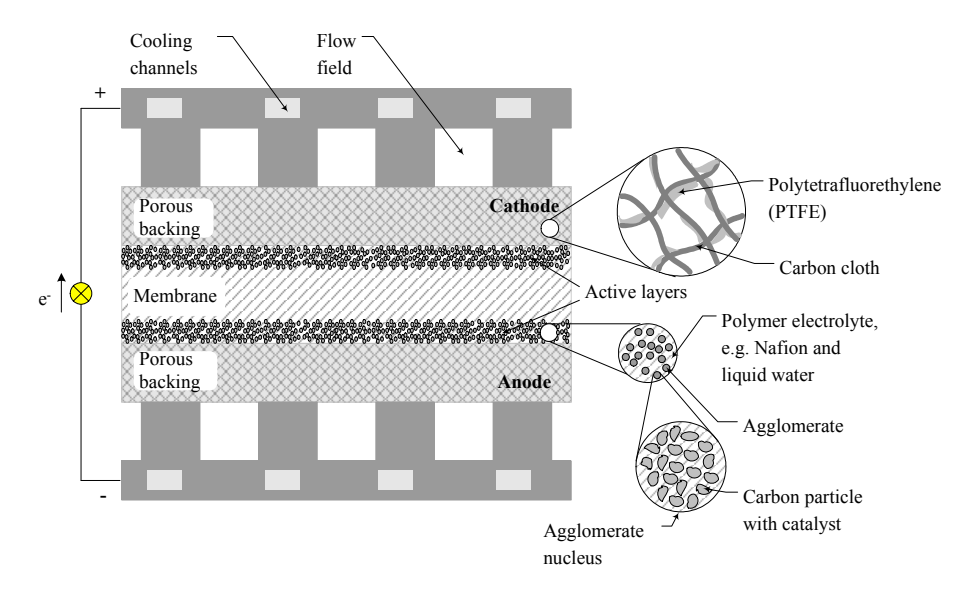


Figure 2.3. A schematic of a cross-section in a fuel cell. Close-ups of the porous backing and active layers are also shown. The active layer is here assumed to contain agglomerates [3].

The main components of the cell are:

Bipolar plate: The electrochemical reactions that occur at the active layers depend on a sufficiently fast transport of reactants to, and products from, the active sites so as to minimize mass transport limitations. Towards this end, the bipolar plates contain grooved channels, which can take a number of different shapes. Amongst the most common designs today are:

- parallel channels, with only one pass over the porous backing, run in coflow.
- parallel channels, with only one pass over the porous backing, run in counterflow.
- interdigitated channels, where channels are terminated, in order to force the flow into the porous backing.
- a porous material, such as a net;

- serpentine flow channels, comprising one long channel with many passes over the porous backing.
- a combination of some of the above.

For the flow fields with channels, the regions between the channels comprise lands⁷, where no fluid flow can occur. The porous flow field, in contrast, covers the whole porous backing due to its porous nature, and thus does not give rise to any 'dead' zones for fluid flow. In addition, coolant channels are usually incorporated in the bipolar plate or added as an extra layer.

Porous backing: The porous backing is made of a composite material, containing carbon cloth/paper and often a hydrophobic agent, such as polytetrafluorethylene. It has to meet many requirements:

- electronic conductivity: The material has to be sufficiently conductive so that the voltage loss is kept at a minimum as well as to facilitate an even current density distribution in the active layers.
- heat conductivity: The heat generated at the active layers has to be removed through the porous backing to the bipolar plate.
- fluid flow permeability: Fluid flow and the mass transfer of reactants to and products from the active layer are crucial for the fuel cell performance.
- wettability: The wettability of the porous backing has to be engineered in such a way that the membrane is kept sufficiently hydrated, whilst simultaneously ensuring that flooding of the porous backing does not occur.
- mechanical stability: The porous backing has to be sufficiently strong to provide support to the MEA as well as keeping the difference in clamping pressure between the land regions and channels at a minimum. If this stability is not ensured, the porous backing might be pushed up into the flow channels and be unduly compressed underneath the lands.

Active layer: The active layers are a porous structure, where contact between the catalyst, usually carbon supported platinum, the electrolyte, the carbon and the reactants has to be provided for, in order to facilitate the electrochemical reactions. For the PEFC, these are

$$2H_2(g) \rightarrow 4H^+ + 4e^-$$
 at the anode, (1)

$$O_2(q) + 4H^+ + 4e^- \rightarrow 2H_2O$$
 at the cathode, (2)

which are termed the hydrogen oxidation reaction (HOR) and the oxygen reduction reaction (ORR), respectively, and for the DMFC:

$$CH_3OH + H_2O \rightarrow CO_2 + 6H^+ + 6e^-$$
 at the anode, (3)

$$CH_3OH + H_2O \rightarrow CO_2 + 6H^+ + 6e^-$$
 at the anode, (3)
 $\frac{3}{2}O_2 + 6H^+ + 6e^- \rightarrow 3H_2O$ at the cathode. (4)

⁷Also referred to as ribs.

The methanol is usually fed as a liquid, whereas the hydrogen is fed as a gas. Note that these reactions are overall reactions, and that in reality, several intermediate reaction steps take place.

Membrane: The membrane, sandwiched between the active layers, comprises a solid polymer, usually Nafion[®], which is a perfluorsulphonic acid polymer. The proton conductivity of the membrane hinges on the humidity level, with a decreasing conductivity for lower humidity levels. It is therefore essential that the membrane is hydrated throughout operation of the fuel cell.

3.1. Literature overview of models for the PEFC. There is an abundance of models available, dealing with both modelling and experiments of the PEFC. Perhaps the first models to provide a simplified treatment of the PEFC were developed by Bernardi and Verbrugge [4,5] and Springer, Zawodzinski and Gottesfeld [6]; a recent contribution is due to Gurau, Barbir and Lui [7]. These models are one-dimensional, and whilst they are able to address some aspects of the three main issues related to fuel cell performance, namely thermal-, water management and mass transfer, they are not able to address these questions at a local level: that is to say, where oxygen depletion occurs, where there is flooding or inadequate heat removal. Subsequent pseudo-two-dimensional models have tackled some of these issues [8–11], with varying assumptions about the nature of the flow; in these so-called 'along-the-channel' models, the resulting equations are ordinary differential equations with the coordinate along the fuel cell as the independent variable. Most recently, techniques of computational fluid dynamics have been used. Amongst models assuming single-phase gaseous flow, there are 2D isothermal models for the cathode [12–14], 2D isothermal models for the whole cell [15–18], and lately three-dimensional models have also begun to appear [14, 19–22, 31]. Dutta, Shimpalee and van Zee considered first a straight channel flow under isothermal conditions [19], followed later by a model for flow in a serpentine channel [20]; most recent work extends [19] to take into account heat transfer for a straight channel flow [21]. Costamagna considers non-isothermal conditions and treats the flow distributor as a porous material [22].

Only a few models, however, exist where also the possibility for liquid water is accounted for [23–32]. He, Yi and Nguyen [23], Natarajan and Nguyen [24], Wang, Wakayama and Okada [25], You and Liu [26], Wang, Wang and Chen [27] focus on the mass transport limitations and water management in a two-dimensional cathode and assume isothermal conditions. All three issues mentioned above, are considered for the whole cell by Djilali and Lu [28], Janssen [29] and Wöhr et al. [30] for a one-dimensional geometry and by Berning and Djilali [31] and Mazumder and Cole [32] for a three-dimensional geometry.

Most of the models are validated on a global scale with polarization curves, which are unable to capture the current density distributions on a local level; only Lum [14] validated her models with both global polarization curves and local current density distributions obtained from a segmented cell.

3.2. Literature overview of models for the DMFC. There are already some models, mostly one-phase, of the DMFC that aim to describe the processes occurring, including the electrochemistry [33–51]. Most of these consider mass transfer in both the gas-backing layer and the active layer [33, 37–41, 44–49, 51], but only a few consider streamwise effects [33, 37, 40, 51].

The carbon dioxide gas is usually neglected in DMFC modelling literature, even though the evolution of gas at the anode can be observed in most practical DMFC applications. Most recently, however, two models considering coexisting gas and liquid phases have been published [50,51]. Wang and Wang [50] apply a multiphase mixture theory for porous media [52] to the porous backings, active layers of both the anode and cathode as well as the membrane of a twodimensional DMFC, and treat the flow channels on the anode side with a fluxdrift model to account for the gas slug flow. They use a simplified expression for the anode kinetics: a Tafel slope with a reaction order that is zero or one depending on the methanol concentration exceeding a threshold value. The model by Divisek et al. [51] is also two-dimensional, but for a cross-section at a given streamwise position and is limited to the porous backings, active layers and membrane of the cell. Common for both these published two-phase models is that they are only validated with global polarization curves, thus lacking any experimental details about the two-phase flow, such as e.g. the amount of gas in the flow channels. Such polarization curves are ill suited for validating the increasing amount of constitutive relations that arise to close the governing equations when proceeding from a one-phase treatment to a model that handles two-phase flow.

CHAPTER 3

Basic concepts

Thus far, the basic principles of fuel cells have been introduced and we have seen that a fuel cell comprises several parts: flow distributors, porous backings, active layers on the anode and cathode side and a membrane. In addition, the available fuel cell technologies of today have been presented, with a more thorough discussion of the PEFC and DMFC. In this chapter, we proceed with the mathematical tools for modelling of the these two fuel cells. The aforementioned parts of the fuel cell have to be modelled and coupled to each other in a convenient way. The porous backings as well as the net-type flow distributors can be treated as porous media, for which volume averaged quantities are employed. We start with the most fundamental definitions of these and continue with the main governing equations for all parts of the fuel cell, both one- and two-phase, that we have used. The treatment of the inherent electrochemistry in the active layers is then summarized.

1. Volume averaging

In a porous medium, see Figure 3.1, the transport processes, such as e.g. conservation of mass and momentum, can be solved on a microscale.

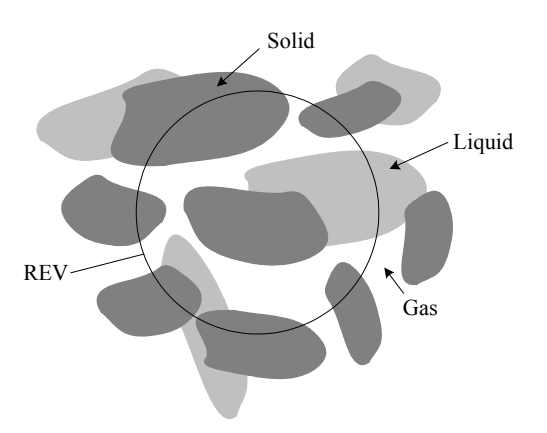


Figure 3.1. A schematic of a porous medium with a gas and liquid phase present and the representative elementary volume (REV).

This, however, requires that we solve for every pore throughout the porous medium, which is computationally expensive as well as time consuming, not to mention that the often complex structure has to be known *a priori*. A more convenient approach is to average the microscale equations over a representative elementary volume (REV), resulting in macroscale equations. For simplicity, we will here assume that we deal with a two-phase system⁸, comprising a liquid (1), a gas (g), and a stationary and rigid solid phase.

For the macroscale description, we define the superficial average of a quantity $\phi^{(k)}$ as

$$\left\langle \phi^{(\mathbf{k})} \right\rangle = \frac{1}{\mathcal{V}} \int_{\mathcal{V}} \phi^{(\mathbf{k})} d\mathcal{V},$$
 (5)

where \mathcal{V} is the total volume of the REV and $\phi^{(k)}$ is the value of the quantity ϕ (scalar, vector, tensor) in phase k (k = l, g). The intrinsic average is defined as

$$\left\langle \phi^{(k)} \right\rangle^{(k)} = \frac{1}{\mathcal{V}^{(k)}} \int_{\mathcal{V}^{(k)}} \phi^{(k)} d\mathcal{V},$$
 (6)

where $\mathcal{V}^{(k)}$ is the volume of phase k in the REV. Introducing the porosity

$$\gamma = \frac{\mathcal{V}^{(g)} + \mathcal{V}^{(l)}}{\mathcal{V}},\tag{7}$$

and the saturation of phase k

$$s^{(k)} = \frac{\mathcal{V}^{(k)}}{\mathcal{V}^{(g)} + \mathcal{V}^{(l)}},\tag{8}$$

the two averages are related through

$$\left\langle \phi^{(k)} \right\rangle = s^{(k)} \gamma \left\langle \phi^{(k)} \right\rangle^{(k)}.$$
 (9)

Here, we have also used that $\phi^{(k)}$ is zero in all the other phases than k. We will retain this notation for the one-phase description of porous flow but omit $\langle . \rangle$ for the corresponding two-phase formulations to save on notation.

2. Governing equations

The main governing equations for the flow distributors and porous backing are summarized below for one- and two-phase flow for the cathode of the PEFC and the anode of the DMFC. For the one-phase flow treatment, we differentiate between plain and porous flow, where the plain flow occurs in the flow channels of the flow field and the porous flow in the porous backing as well as in the flow field, if a net-type flow distributor is used. For the two-phase flow, we will list the governing equations for a separate flow (PEFC, Paper 3 and 4) and a multiphase mixture (DMFC, Paper 7) approach. For brevity, we refer to the papers for the constitutive relations and boundary conditions, which together with the governing equations constitute closed systems.

⁸The term "two-phase", referring to the mobile liquid and gas phase, is somewhat misleading, since we actually consider three phases.

For the PEFC, the flow will remain gas-phase as long as the water vapor pressure does not exceed the saturation pressure, whereas for a liquid-fed DMFC, the flow will be in liquid form until the carbon dioxide stemming from the oxidation at the active layer evolves as gas. A model based on one-phase flow will thus not be able to account for the liquid water (PEFC) or the gas (DMFC), but can nonetheless give valuable information (Paper 1, 2 and 5).

2.1. Plain Flow. The flow distributor can take many shapes, depending on the requirements of the fuel cell: flow channels machined into a bipolar plate, comprising e.g. interdigitated, parallel or serpentine channels. In the flow channels, we solve for continuity of mass and momentum, given by

$$\nabla \cdot (\rho \mathbf{v}) = 0, \tag{10}$$

$$\nabla \cdot (\rho \mathbf{v} \otimes \mathbf{v}) = -\nabla \left(p + \frac{2}{3} \mu \nabla \cdot \mathbf{v} \right) + \nabla \cdot \left(\mu \left((\nabla \mathbf{v}) + (\nabla \mathbf{v})^{\mathrm{T}} \right) \right), \tag{11}$$

where \mathbf{v} is the velocity, ρ is the density, p is the pressure and μ is the dynamic viscosity. The transport equations for the ternary gas mixture, comprising oxygen, water and nitrogen are

$$\nabla \cdot \left(\rho \mathbf{v} \begin{pmatrix} w_{\mathrm{O}_{2}} \\ w_{\mathrm{H}_{2}\mathrm{O}} \end{pmatrix} \right) = \nabla \cdot \left(\rho \mathbf{D} \begin{bmatrix} \nabla w_{\mathrm{O}_{2}} \\ \nabla w_{\mathrm{H}_{2}\mathrm{O}} \end{bmatrix} \right), \tag{12}$$

where w_{O_2} and $w_{\text{H}_2\text{O}}$ are the mass fractions of oxygen and water and **D** is the diffusion tensor. To obtain the corresponding formulation for the DMFC, substitute $MeOH = O_2$, $CO_2 = H_2O$.

2.2. Porous flow. Conservation of mass and momentum in the porous backing or in a net-type flow field is given respectively by

$$\nabla \cdot \left(\langle \rho \rangle^{(g)} \langle \mathbf{v} \rangle \right) = 0, \tag{13}$$

$$\nabla \cdot \left(\langle \rho \rangle^{(g)} \langle \mathbf{v} \rangle \otimes \langle \mathbf{v} \rangle \right) + \mu \mathbf{K}^{-1} \cdot \langle \mathbf{v} \rangle = -\nabla \left(\langle p \rangle^{(g)} + \frac{2}{3} \frac{\mu}{\gamma} \nabla \cdot \langle \mathbf{v} \rangle \right) + \nabla \cdot \left(\frac{\mu}{\gamma} \left(\nabla \langle \mathbf{v} \rangle + (\nabla \langle \mathbf{v} \rangle)^{\mathrm{T}} \right) \right), \quad (14)$$

where \mathbf{K} is the permeability tensor. An alternative formulation for conservation of momentum is Darcy's law with the Forchheimer and Brinkman extension

$$\langle \mathbf{v} \rangle = -\frac{\kappa}{\mu} \nabla \langle p \rangle^{(g)} + \kappa \nabla^2 \left(\frac{\langle \mathbf{v} \rangle}{\gamma} \right) - \mathbf{F} \langle \mathbf{v} \rangle, \qquad (15)$$

where \mathbf{F} is the Forchheimer correction tensor.

The species transport equations are described by

$$\nabla \cdot \left(\langle \rho \rangle^{(g)} \langle \mathbf{v} \rangle \begin{pmatrix} \langle w_{\mathcal{O}_2} \rangle^{(g)} \\ \langle w_{\mathcal{H}_2 \mathcal{O}} \rangle^{(g)} \end{pmatrix} \right) = \nabla \cdot \left(\langle \rho \rangle^{(g)} \gamma \langle \mathbf{D} \rangle^{(g)} \begin{bmatrix} \nabla \langle w_{\mathcal{O}_2} \rangle^{(g)} \\ \nabla \langle w_{\mathcal{H}_2 \mathcal{O}} \rangle^{(g)} \end{bmatrix} \right), \tag{16}$$

where $\langle \mathbf{D} \rangle^{(g)}$ is the total mass diffusion tensor, containing contributions from an intrinsic effective mass diffusion tensor and an intrinsic hydrodynamic dispersion tensor. For a more detailed discussion of these, see paper 1. To obtain the corresponding formulation for the DMFC, substitute $MeOH = O_2$, $CO_2 = H_2O$ and (l) = (g).

2.3. Conservation of charge. Conservation of charge together with Ohm's law gives

$$\nabla^2 \phi = 0, \tag{17}$$

where ϕ is the electric potential of the solid phase in the porous backings or the ionic phase in the membrane. This equation constitutes a simplification of the proton transport in the membrane.

2.4. Separate flow model. The PEFC is usually operated at high relative humidities or even at two-phase conditions since the membrane conductivity hinges on the membrane being sufficiently hydrated. To account for a liquid phase in addition to the gas phase, we apply a separate flow model (Paper 3 and 4), where we treat the liquid and gas phase as immiscible.

The solubility of nitrogen and oxygen is sufficiently small to allow the liquid phase to be treated as pure liquid water. In the porous backing of the cathode, we solve for the conservation of mass and momentum of the liquid and gas phase:

$$\nabla \cdot \left(\rho^{(g)} \mathbf{v}^{(g)}\right) = -\dot{m}_{H_2O}, \tag{18}$$

$$\nabla \cdot \left(\rho^{(l)} \mathbf{v}^{(l)}\right) = \dot{m}_{H_2O}, \tag{19}$$

$$\nabla \cdot \left(\rho^{(1)} \mathbf{v}^{(1)} \right) = \dot{m}_{\mathrm{H}_2\mathrm{O}}, \tag{19}$$

$$\nabla p^{(g)} = -\frac{\mu^{(g)}}{\kappa \kappa_{\text{rel}}^{(g)}} \mathbf{v}^{(g)}, \qquad (20)$$

$$\nabla p^{(1)} = -\frac{\mu^{(1)}}{\kappa \kappa_{\text{rel}}^{(1)}} \mathbf{v}^{(1)}, \qquad (21)$$

where $\rho^{(g,l)}$ denote the phase densities, $\mathbf{v}^{(g,l)} = (u^{(g,l)}, v^{(g,l)})$ are the phase velocities, $\dot{m}_{\rm H_2O}$ is the interface mass transfer of water between the gas and liquid phase, $p^{(g,l)}$ are the phase pressures, $\mu^{(g,l)}$ are the phase dynamic viscosities, κ is the permeability and $\kappa_{\rm rel}^{({\rm g},l)}$ are the relative permeabilities of the phases. In addition, we solve for a ternary mixture of water, nitrogen and oxygen

in the gas phase

$$\nabla \cdot \begin{bmatrix} \mathbf{n}_{O_2}^{(g)} \\ \mathbf{n}_{H_2O}^{(g)} \end{bmatrix} + \begin{bmatrix} 0 \\ \dot{m}_{H_2O} \end{bmatrix} = 0, \tag{22}$$

with the componential mass fluxes

$$\begin{bmatrix} \mathbf{n}_{\text{O}_{2}}^{(g)} \\ \mathbf{n}_{\text{H}_{2}\text{O}}^{(g)} \end{bmatrix} = \rho^{(g)} \mathbf{v}^{(g)} \begin{bmatrix} w_{O_{2}}^{(g)} \\ w_{H_{2}\text{O}}^{(g)} \end{bmatrix} - \rho^{(g)} \gamma^{\frac{3}{2}} (1 - s) \mathbf{D}^{(g)} \begin{bmatrix} \nabla w_{O_{2}}^{(g)} \\ \nabla w_{H_{2}\text{O}}^{(g)} \end{bmatrix}, \quad (23)$$

where $\mathbf{D}^{(\mathrm{g})}$ is a multicomponent mass diffusion tensor, γ is the porosity, s is the liquid saturation and $w_{\mathrm{H}_2\mathrm{O}}^{(\mathrm{g})}$ and $w_{\mathrm{O}_2}^{(\mathrm{g})}$ are the mass fraction of water and oxygen in the gas phase, respectively. The heat transfer is given by

$$-\nabla \cdot (k_{\rm c} \nabla T) = H_{\rm vap} \dot{m}_{\rm H_2O} + \sigma_{\rm c} (\nabla \phi_{\rm s})^2; \qquad (24)$$

here T is the temperature (assuming thermal equilibrium), $k_{\rm c}$ is a thermal conductivity and $H_{\rm vap}$ is the enthalpy of vaporization. The terms on the RHS of Eq. 24 account for the heat of vaporization and ohmic heating. Note that the convective heat transfer has been omitted in Eq. 24, since this term was found to be negligible compared to the heat conduction (Paper 3 and 4).

The governing equations are simplified by removing the liquid pressure via the definition of the capillary pressure $p^{(c)} \equiv p^{(g)} - p^{(l)}$, in the two-phase region. By taking the gradient of the capillary pressure, and combining Eqs. 20 and 21, the liquid velocity is obtained:

$$\mathbf{v}^{(1)} = \mathbf{m}\mathbf{v}^{(g)} - D^{(c)}\nabla s,\tag{25}$$

where \mathfrak{m} is the mobility of the liquid phase and $D^{(c)}$ can be viewed as a capillary diffusion coefficient

$$\mathfrak{m} = \frac{\kappa_{\text{rel}}^{(1)} \mu^{(g)}}{\kappa_{\text{rel}}^{(g)} \mu^{(1)}}, \tag{26}$$

$$D^{(c)} = -\frac{\kappa \kappa_{\rm rel}^{(1)}}{\mu^{(1)}} \frac{dp^{(c)}}{ds}.$$
 (27)

It is assumed that the capillary pressure is only a function of saturation; $p^{(c)} = p^{(c)}(s)$.

2.5. Multiphase mixture model. For a liquid-fed anode, the flow through the anode will remain liquid as long as no current is drawn from the cell. As soon as a current is drawn, carbon dioxide is produced from the oxidation reaction at the active layer of the anode. Provided that the carbon dioxide partial pressure is sufficiently high and nucleation can occur, gas will evolve. Usually, the liquid dilute methanol/water mixture fuel is recirculated, whence the entering liquid fuel is saturated with carbon dioxide. Incorporating these effects calls for a two-phase model, where conservation of mass, momentum and species are treated (Paper 7). For this purpose, we apply a multiphase mixture formulation for porous flow, derived by [52]. The ternary gas and liquid phases are assumed to be in equilibrium, comprising carbon dioxide, methanol and water.

We solve for the continuity of mass and momentum of the liquid and gas phase

$$\nabla \cdot (\rho \mathbf{v}) = 0, \tag{28}$$

$$\nabla p = -\frac{\mu}{\kappa} \mathbf{v} + \rho_{\mathbf{k}} \mathbf{g},\tag{29}$$

where ρ , \mathbf{v} , p, μ and ρ_k are the mixture density, the mixture velocity, the mixture pressure, mixture dynamic viscosity and kinematic mixture density, respectively, κ is the absolute permeability and \mathbf{g} is the gravity. When referring to the properties of the individual liquid and gas phases, we will use the superscripts (1) and (g), respectively. The mixture variables are defined as

$$\rho = \rho^{(1)}s + \rho^{(g)}(1-s), \tag{30}$$

$$\rho_{k} = \lambda^{(1)} \rho^{(1)} + \lambda^{(g)} \rho^{(g)},$$
(31)

$$\rho \mathbf{v} = \rho^{(1)} \mathbf{v}^{(1)} + \rho^{(g)} \mathbf{v}^{(g)}, \tag{32}$$

$$\mu = \frac{\rho^{(1)}s + \rho^{(g)}(1-s)}{\rho^{(1)}\kappa_{\text{rel}}^{(1)}/\mu^{(1)} + \rho^{(g)}\kappa_{\text{rel}}^{(g)}/\mu^{(g)}},$$
(33)

$$\lambda^{(l)} = \frac{\rho^{(l)} \kappa_{\rm rel}^{(l)} / \mu^{(l)}}{\rho^{(l)} \kappa_{\rm rel}^{(l)} / \mu^{(l)} + \rho^{(g)} \kappa_{\rm rel}^{(g)} / \mu^{(g)}}, \tag{34}$$

$$\lambda^{(g)} = 1 - \lambda^{(l)}. \tag{35}$$

The superficial phase velocities of the liquid and gaseous phase can be found from the relations

$$\rho^{(1)}\mathbf{v}^{(1)} = \frac{\lambda^{(1)}\lambda^{(g)}\kappa\rho}{\mu} \left(\nabla p^{(c)} + \left(\rho^{(1)} - \rho^{(g)}\right)\mathbf{g}\right) + \lambda^{(1)}\rho\mathbf{v}, \tag{36}$$

$$\rho^{(g)}\mathbf{v}^{(g)} = -\frac{\lambda^{(1)}\lambda^{(g)}\kappa\rho}{\mu} \left(\nabla p^{(c)} + \left(\rho^{(1)} - \rho^{(g)}\right)\mathbf{g}\right) + \lambda^{(g)}\rho\mathbf{v}.$$
(37)

Species transfer is accounted for by

$$\nabla \cdot \begin{bmatrix} \mathbf{N}_{\text{MeOH}} \\ \mathbf{N}_{\text{CO}_2} \end{bmatrix} = 0, \tag{38}$$

with

$$\begin{bmatrix}
\mathbf{N}_{\text{MeOH}} \\
\mathbf{N}_{\text{CO}_{2}}
\end{bmatrix} = \rho \mathbf{v} \left(\frac{\lambda^{(l)}}{M^{(l)}} \begin{bmatrix} x_{\text{MeOH}}^{(l)} \\ x_{\text{CO}_{2}}^{(l)} \end{bmatrix} + \frac{\lambda^{(g)}}{M^{(g)}} \begin{bmatrix} x_{\text{MeOH}}^{(g)} \\ x_{\text{CO}_{2}}^{(g)} \end{bmatrix} \right) - \left(\frac{s\rho^{(l)}\gamma \langle \mathbf{M} \rangle^{(l)}}{(M^{(l)})^{2}} \begin{bmatrix} \nabla x_{\text{MeOH}}^{(l)} \\ \nabla x_{\text{CO}_{2}}^{(l)} \end{bmatrix} + \frac{(1-s)\rho^{(g)}\gamma \langle \mathbf{M} \rangle^{(g)}}{(M^{(g)})^{2}} \begin{bmatrix} \nabla x_{\text{MeOH}}^{(g)} \\ \nabla x_{\text{CO}_{2}}^{(g)} \end{bmatrix} \right) + \left(\frac{1}{M^{(l)}} \begin{bmatrix} x_{\text{MeOH}}^{(l)} \\ x_{\text{CO}_{2}}^{(l)} \end{bmatrix} - \frac{1}{M^{(g)}} \begin{bmatrix} x_{\text{MeOH}}^{(g)} \\ x_{\text{CO}_{2}}^{(g)} \end{bmatrix} \right) \frac{\lambda^{(l)}\lambda^{(g)}\kappa\rho}{\mu} \left(\nabla p^{(c)} + \left(\rho^{(l)} - \rho^{(g)} \right) \mathbf{g} \right); \tag{39}$$

here, \mathbf{N}_{MeOH} and \mathbf{N}_{CO_2} are the total molar fluxes of methanol and carbon dioxide, $\langle \mathbf{M} \rangle^{(l,g)}$, $\lambda^{(l)}$ and $\lambda^{(g)}$ are the diffusion tensors and mobilities of the liquid and gas phase, respectively, $p^{(c)}$ is the capillary pressure, $p^{(g)}$ is the pressure in the gas phase, $\rho^{(k)}$ and $x_i^{(k)}$ are the density and molar fractions of species i of phase k, respectively.

The capillary pressure is defined as

$$p^{(c)} = p^{(g)} - p^{(l)}, (40)$$

and the mixture pressure

$$\nabla p = \nabla p^{(1)} + \lambda^{(g)} \nabla p^{(c)}. \tag{41}$$

3. Electrokinetics and the active layers

The active layers are not resolved, but rather treated as boundary or interface conditions. For the DMFC (Paper 5 and 7), however, the changes in potential and concentration inside the active layer of the anode are still accounted for and can, if so desired, be computed a posteriori.

3.1. Polymer electrolyte fuel cell. In paper 1, a Tafel law given by [54] was applied for the current density at the cathode

$$i = \frac{a\rho}{M} \exp\left(\frac{\alpha_{\rm c} F \eta_{\rm c}}{RT}\right),\tag{42}$$

where α_c is the transfer coefficient of the oxygen reduction reaction, η_c is the overpotential for the oxygen reaction (defined positive) and a is a constant related to the exchange current density and oxygen reference concentration for the ORR.

In paper 2, the volumetric current density $i_{\rm v}$ for the cathode, given by [3], was approximated as

$$i_{\rm v} = \mathcal{A}i_{0,\rm c} \left(1 - \gamma_{\rm pol}\right) \left(1 - \gamma_{\rm active}\right) \exp\left(-\frac{\alpha_{\rm r}F}{RT}\eta_{\rm c}\right) \mathfrak{F}\frac{c_{\rm O_2}^{\rm (g)}}{c_{\rm O_2}^{\rm ref}}$$
 (43)

where $\mathcal{A}i_{0,\mathrm{c}}$ is the volumetric exchange current density in the agglomerates, γ_{pol} is the volume fraction of the polymer electrolyte in the agglomerate nucleus, $c_{\mathrm{O}_2}^{(\mathrm{g})} = w_{\mathrm{O}_2}^{(\mathrm{g})} \rho^{(\mathrm{g})}/M_{\mathrm{O}_2}$ is the molar concentration of oxygen, α_{r} is the cathodic transfer coefficient for the ORR, n is the number of electrons consumed in the ORR per oxygen molecule, η_{c} is the overpotential at the cathode (defined negative), and γ_{active} is the volume fraction of pores in the active layer. \mathfrak{F} is the nucleus effectiveness factor, defined as

$$\mathfrak{F} = \frac{3}{\Upsilon r} \left(\frac{1}{\tanh(\Upsilon r)} - \frac{1}{\Upsilon r} \right),\tag{44}$$

with Υ given by

$$\Upsilon = \sqrt{\frac{\mathcal{A}i_0 \left(1 - \gamma_{\rm p}\right) \exp\left(-\frac{\alpha_{\rm r}F}{RT}\eta\right)}{nF\mathfrak{D}}},\tag{45}$$

where \mathfrak{D} is an effective oxygen permeability in the agglomerates and r is the radius of the agglomerate nucleus. This agglomerate model was validated by [53] for a small PEFC with an area of 2 cm². The total current density is then locally given by $i_{\rm c}=i_{\rm v}h_{\rm active}$. Jaouen et al. [3] discerned four different regimes, where the Tafel slope doubles or even quadruples, and subsequently supplied the experimental validation to support these [53]. In regime 1, the active layer

is controlled by Tafel kinetics and is first order in the oxygen concentration. Regime 2 displays a doubling of the Tafel slope, due to the active layer being governed by Tafel kinetics and oxygen diffusion in the agglomerates, but still remains first order in the oxygen concentration. A doubling of the Tafel slope is observed in the third regime, where the active layer is controlled by the Tafel kinetics, in addition to proton migration. The oxygen dependence here is half-order. The final regime, the fourth, shows a quadrupling of the Tafel slope, and is attributable to an active layer controlled by Tafel kinetics, proton migration and oxygen diffusion in the agglomerates. The oxygen dependence is half-order, as in regime 3.

In paper 3, we tried to adapt the agglomerate model to a polarization curve obtained from a segmented cell, equipped with a net-type flow field, but it turned out that the agglomerate model reduced to

$$i_{\rm c} = \zeta_1 (1 - s) x_{\rm O_2}^{\rm (g)} \exp(-\zeta_2 \eta_{\rm c}),$$
 (46)

where ζ_1 and ζ_2 are the two parameters adapted. Essentially this mean that the nucleus effectiveness factor $\mathfrak{F}=1$, which we surmise is due to the thin MEA (Gore Primea 5510) that was used in the segmented cell. In paper 4, the parameter adapted current density was also applied.

3.2. Direct methanol fuel cell. In paper 5, an expression for the current density was found from parameter-adaption to experimental data [55]

$$\langle i \rangle = A \left(\langle c_{\text{MeOH}} \rangle^{(1)} \right)^B \frac{\exp\left(\frac{\alpha_{\text{A}} F}{RT} \left(E_{\text{A}} - E_0 \right) \right)}{1 + \exp\left(\frac{\alpha_{\text{A}} F}{RT} \left(E_{\text{A}} - E_0 \right) \right)}. \tag{47}$$

Figure 3.2 shows that this expression for the local current density correlates well to the data from the electrode model [55] for $0.3\text{V} \le E \le 0.51 \text{ V}$ and 50 mol m⁻³ $\le \langle c_{\text{MeOH}} \rangle^{(1)} \le 1000 \text{ mol m}^{-3}$.

In paper 7, the current density at the active layer is given [56], as

$$i(x_{\text{MeOH}}^{(1)}, T, M^{(1)}, E_{\text{A}}) = \frac{\exp\left(\frac{\alpha_{\text{A}}F}{RT} \left(E_{\text{A}} - \mathfrak{E}_{\text{A}}\right)\right)}{1 + \frac{\exp\left(\frac{\alpha_{\text{A}}F}{RT} \left(E_{\text{A}} - \mathfrak{E}_{\text{A}}\right)\right)}{i_{\text{line}}}},$$
(48)

$$\mathfrak{E}_{\mathbf{A}} = \mathfrak{c}_1 - \mathfrak{c}_2 T, \tag{49}$$

$$i_{\text{lim}} = \tanh\left(\frac{x_{\text{MeOH}}^{(1)}\Big|_{y=-h_{\text{p}}}\rho^{(1)}}{M^{(1)}\Big|_{y=-h_{\text{p}}}\mathfrak{c}_{3}}\right)\left(\frac{E_{\text{A}}}{\mathfrak{c}_{4}}\right)^{\vartheta}\left(\mathfrak{c}_{5}T^{2}-\mathfrak{c}_{6}T+\mathfrak{c}_{7}\right), \quad (50)$$

$$\vartheta = \mathfrak{c}_8 \tanh \left(\frac{x_{\text{MeOH}}^{(l)} \Big|_{y=-h_p} \rho^{(l)}}{M^{(l)} \Big|_{y=-h_p} \mathfrak{c}_9} \right), \tag{51}$$

where *i* is the local current density, $E_{\rm A}$ is the anode potential measured at the active layer/membrane interface versus a reference electrode ($E_{\rm A}=0.2-0.7~{\rm V}$ [56]), $\alpha_{\rm A}$ is a measured Tafel slope, and $\mathfrak{c}_{\rm i}$ are experimentally fitted parameters.

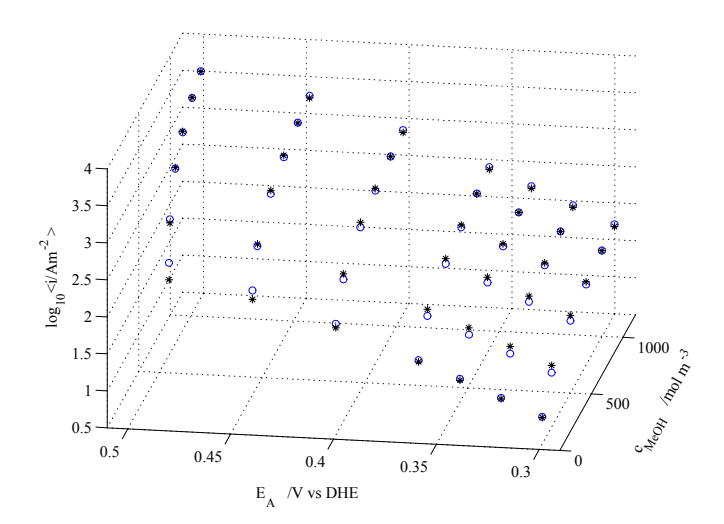


Figure 3.2. Comparison between the parameter-adapted kinetic function (o), used as local superficial current density for the boundary conditions at $(0 \le X \le 1, Y = -\mathcal{H})$, and the result from the more detailed anode model [55] (*).

The kinetic equation, Eq. 48, is taken from an earlier work [56] and includes losses in the porous electrodes, such as limited ionic conductivity and limitations in mass transfer. The equation is valid in the range 303-343 K and $100\text{-}4000 \text{ mol m}^{-3}$ methanol concentration and is validated against experimental data.

4. Scale analysis and nondimensional numbers

Nondimensionalization and scale analysis of the governing equations often allows a considerable simplification of these, where the main governing parameters as well as magnitude of transport mechanisms can be derived a priori to any computations. The geometry ratio of the fuel cell is such that the ratio of the heights of the flow channel, porous backing and active layer to the length is much smaller than one. This slenderness, captured by introducing $\sigma = h/L$, where h is the height, can be exploited, yielding reduced formulations (Paper 1, 5 and 7).

Let $[\mu]$, U, L, $|\mathfrak{p}|$, $[\rho]$, $[c_p]$, [i], [M] and [D] denote typical scales for the dynamic viscosity, the velocity, the length, the capillary pressure, the density, the specific heat at constant pressure, the current density, the mean molecular mass and the diffusion, respectively. The main dimensionless numbers are then the capillary number

$$Ca \equiv \frac{[\mu]UL}{|\mathfrak{p}| \, \kappa} \, \left(\frac{\text{Viscous pressure drop}}{\text{Capillary pressure}} \right),$$

the Damköhler numbers (F is Faraday's constant)

$$\begin{array}{lll} \Lambda & \equiv & \frac{[i][M]}{[\rho]UF} \left(\frac{\text{Reaction rate}}{\text{Mass transport rate}} \right), \\ \Omega & \equiv & \frac{\Lambda}{\sigma} \left(\frac{\text{Reaction rate}}{\text{Mass transport rate}} \right), \end{array}$$

the Darcy number

$$Da \equiv \frac{\kappa}{L^2} \text{ (Dimensionless permeability)},$$

the reciprocal of the reduced Reynolds number

$$\Delta \equiv \frac{1}{\text{Re}\,\sigma^2}$$

the Froude number

$$Fr \equiv \frac{U^2}{gL} \left(\frac{Inertia force}{Gravity force} \right),$$

the gravillary number

$$\mathrm{Gl} \equiv \frac{\rho^{(1)}gl}{|\mathfrak{p}|} \; \left(\frac{\mathrm{Gravitational\ pressure}}{\mathrm{Capillary\ pressure}}\right),$$

the gravitary number

$$\mathrm{Gr} \equiv \frac{[\mu]U}{[\rho]g\kappa} \; \left(\frac{\mathrm{Viscous\;pressure\;drop}}{\mathrm{Gravitational\;pressure}} \right),$$

the Peclet number for heat transfer

$$Pe^{(heat)} \equiv \frac{U[\rho]L[c_p]}{k} \quad \left(\frac{\text{Heat convection}}{\text{Heat conduction}}\right),$$

and mass transfer

$$\mathrm{Pe^{(mass)}} \equiv \frac{UL}{[D]} \; \left(\frac{\mathrm{Bulk \; mass \; transfer}}{\mathrm{Diffusive \; mass \; transfer}} \right),$$

the Reynolds number

$$\mathrm{Re} \equiv \frac{[\rho]LU}{[\mu]} \; \left(\frac{\mathrm{Inertia\ force}}{\mathrm{Viscous\ force}} \right),$$

the Schmidt number

$$Sc \equiv \frac{[\mu]}{[\rho][D]} \left(\frac{\text{Momentum diffusivity}}{\text{Mass diffusivity}} \right).$$

5. Numerical tools and methodologies

To solve the mathematical models for the PEFC and DMFC, various methods were adopted, a summary of which is given below.

- **5.1.** Keller Box discretization scheme. Invoking the slenderness of the fuel cells, the elliptic governing equations were reduced to parabolic for a cross-section in the normal and streamwise directions, for which the Keller Box discretization scheme [57] is suitable (Paper 1 and 7). The scheme leads to a block tridiagonal matrix, allowing fast computations. The resulting system of non-linear equations is solved with a Newton-Raphson-based algorithm in MATLAB 6 (see [58] for details).
- **5.2.** Modified Box discretization method. The Modified Box discretization scheme [59] is a reduced version of the aforementioned Keller Box, and requires more effort to derive (Paper 7). The scheme leads to a block tridiagonal matrix, allowing fast computations. The resulting system of non-linear equations is solved with a Newton-Raphson-based algorithm in MATLAB 6.
- **5.3. Femlab 2.3.** FEMLAB 2.3 (see [60] for details), is a commercial finite element solver for a wide variety of engineering applications. It was used to verify several of the reduced DMFC models (Paper 5 and 7) as well as model a cross-section in the normal and spanwise directions for the PEFC (Paper 3 and 4).
- **5.4. CFX 4.4.** A commercial computational fluid dynamics code, CFX-4.4 (see [61] for details), based on finite volumes, was used for three dimensional computations of various flow fields (Paper 2), as well as for verification of a reduced model (Paper 5).
- **5.5.** Maple 7. Maple 7 (see [62] for details) was used to secure closed form solutions for the asymptotic analyses, to produce Fortran code and to find analytical solutions, where applicable.

CHAPTER 4

Summary of results

1. Polymer electrolyte fuel cells

Four models for the cathode have been derived and analyzed. The first (Paper 1) sees the derivation of a gas phase isothermal 2-D model for conservation of mass, momentum and species for the cathode followed by nondimensionalization and an asymptotic analysis. The fact that the geometry is slender, see Figure 4.1, allows the use of a narrow-gap approximation, leading to a simplified formulation.

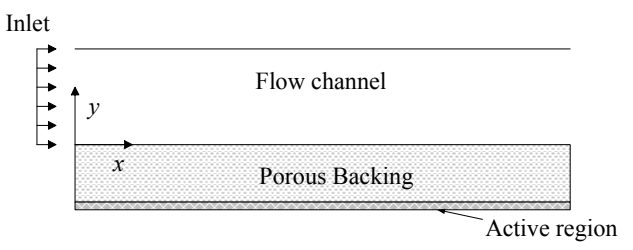


Figure 4.1. A schematic of the cathode.

Inspite of the highly non-linear coupling between the velocity variables and the mole fractions, an asymptotic treatment of the problem indicates that oxygen consumption and water production can be described rather simply in the classical lubrication theory limit with the reduced Reynolds number as a small parameter. In general, however, the reduced Reynolds number is O(1), requiring a numerical treatment; this is done using the Keller-Box discretization scheme. The analytical and numerical results are compared in the limit mentioned above, and further results are generated for varying inlet velocity and gas composition, channel width and porous backing thickness, pressure and current density. In addition, polarization surfaces, constituting a novel, compact way to present fuel cell performance, which take into account geometrical, hydrodynamical and electrochemical features, are introduced. One such polarization surface is shown in Figure 4.2 for varying inlet molar fractions of oxygen and water, from which it is clear, that the greater the oxygen content in the gas stream at the inlet of the cathode, the greater will be the current density.

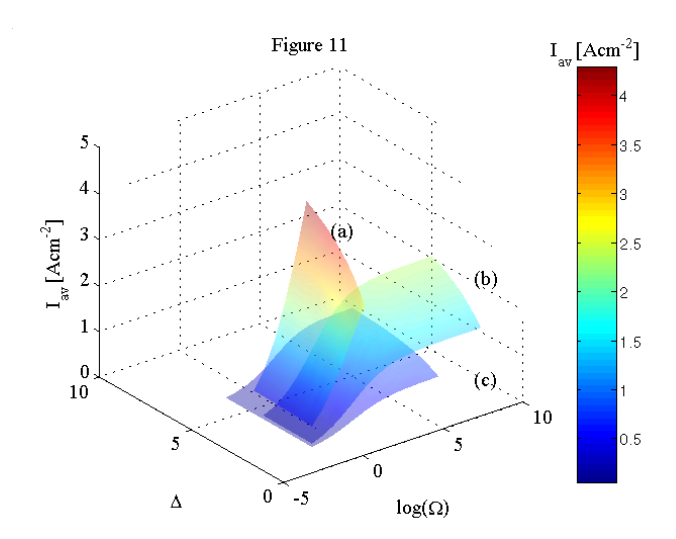


Figure 4.2. Polarization surfaces for $p^{\text{out}}=1$ atm with: (a) $x_{\text{O}_2}^{\text{in}}=1$, $x_{\text{H}_2\text{O}}^{\text{in}}=0$; (b) $x_{\text{O}_2}^{\text{in}}=0.21$, $x_{\text{H}_2\text{O}}^{\text{in}}=0$; (c) $x_{\text{O}_2}^{\text{in}}=0.13$, $x_{\text{H}_2\text{O}}^{\text{in}}=0.36$.

The second model (Paper 2) is similar to the first, with the important distinction that it is extended to account for a fully three dimensional cathode. The aim of this model was to compare the performance of different flow distributors (parallel coflow, parallel counterflow, interdigitated, foam) for a given cell at a given potential, in terms of four different quantities: the obtained average current density, power density, standard deviation of the current density distribution and pressure drop. The results show that the interdigitated flow distributor can sustain the highest current densities, as depicted in Figure 4.3, but at a higher pressure drop than the counterflow and coflow channels. Furthermore, to function properly, the interdigitated channels would have to be in contact with the porous backing in such a way that channeling effects are kept at a minimum; given the high velocities required, even the slightest gap might lead to most of the flow going through the gap and not through the porous backing, with a resulting loss of power density. A foam distributor is able to give the lowest standard deviation for the current at high current densities, but care should be taken as to its permeability to avoid an unreasonably high pressure drop.

These two models (Paper 1 and 2) are limited to gas-phase flow and isothermal conditions. Non-isothermal effects and the liquid water were added via a separate flow model (Paper 3) for a two-dimensional cross-section, see Figure 2.3.

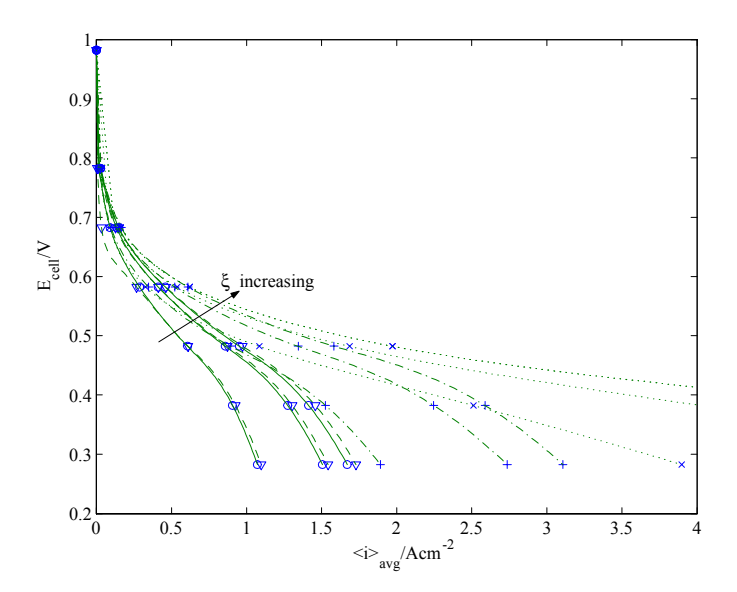


Figure 4.3. Polarisation curves for the different flow distributors at stoichiometry $\xi = 1.5$, 3, 5: coflow channels (o), counterflow channels (∇) , interdigitated channels (x), foam (+).

This model is then analyzed and solved numerically under three different thermal and two hydrodynamic modelling assumptions:

- a) an effective heat conductivity with a capillary pressure of $O(10^4)$ Nm⁻² in the porous backings [27];
- b) isothermal conditions with a capillary pressure of $O(10^4) \text{ Nm}^{-2}$ in the porous backings [27];
- c) thermal bulk and contact resistances with a capillary pressure of $O(10^4) \text{ Nm}^{-2}$ in the porous backings [27];
- d) an effective heat conductivity with an alternative capillary pressure of O(40) Nm⁻² in the porous backings [24];

The consequences of these are then discussed in terms of thermal and water management and cell performance. The study is motivated by recent experimental results that suggest the presence of previously unreported, and thus unmodeled, thermal contact resistances between the components of a PEFC [63], and the discrepancy in the value for the capillary pressure that is used by different authors when modelling the two-phase flow in a PEFC. In the three cases that deal with varying thermal conditions (a-c), see Figure 4.4, liquid saturations of around 10% are obtained at the cathode active layer for 1000 mAcm $^{-2}$ and a cell voltage of 0.6 V, in contrast to almost 50 % (locally up to 100%) for case d, where the alternative capillary pressure is considered. For the first

three cases, the liquid water removal is sufficiently fast to avoid flooding of the cathode, whereas for the latter, the capillary forces for the water removal are too weak, leading to a partially flooded active layer, causing a reduction in the current density and hence also in the heat production.

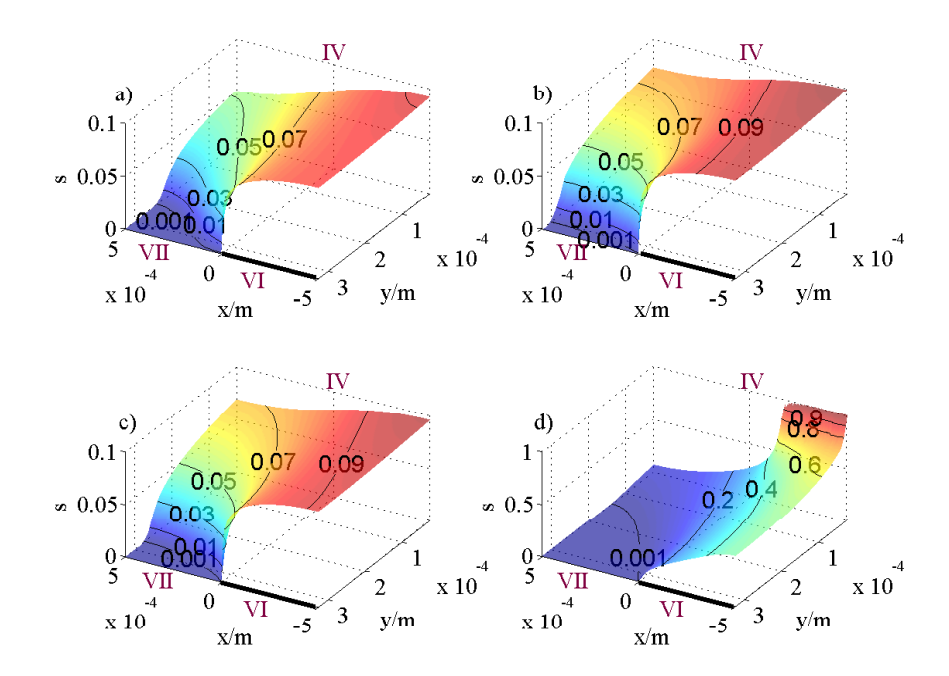


Figure 4.4. Liquid saturation distributions ($E^{\text{cell}} = 0.6 \text{ V}$): a) effective thermal conductivity; b) isothermal; c) thermal bulk and contact conductivities; d) alternative capillary pressure.

This decrease in heat production leads to the decrease in temperature in the spanwise direction, as depicted in Figure 4.5c. For cases a-c, the capillary pressure is of the order of 10^4 Nm⁻², thus constituting a higher driving force for the liquid water than for case d, where the capillary pressure is around 40 Nm^{-2} .

As can be inferred from Figure 4.5, the temperature is highest at the cathode side of the membrane, due to the exothermic ORR, and drops off towards the current collector ribs, which are kept at a constant temperature $T^{\rm cool}=60^{\rm o}$ C. For case a, where the effective thermal conductivity is considered, the drop in temperature occurs throughout the porous backings and the membrane, amounting to a temperature difference of 4.5°C. In case c, where the heat conductivity comprises both a bulk and an interface conductivity,

most of the temperature loss takes place at the interfaces between the current collectors and porous backings and porous backings and membrane. The overall temperature increase is here also 4.5° C: with $\sim 1^{\circ}$ C increase across the porous backings; $\sim 1^{\circ}$ C increase at the interface between the current collectors and the porous backings; $\sim 2.5^{\circ}$ C increase at the interface between the porous backing and the membrane on the cathode side and a corresponding increase of $\sim 1^{\circ}$ C at the anode. Furthermore, the characteristic cell performance quantities, such as temperature increase and current density, could be predicted prior to computations via a scale analysis.

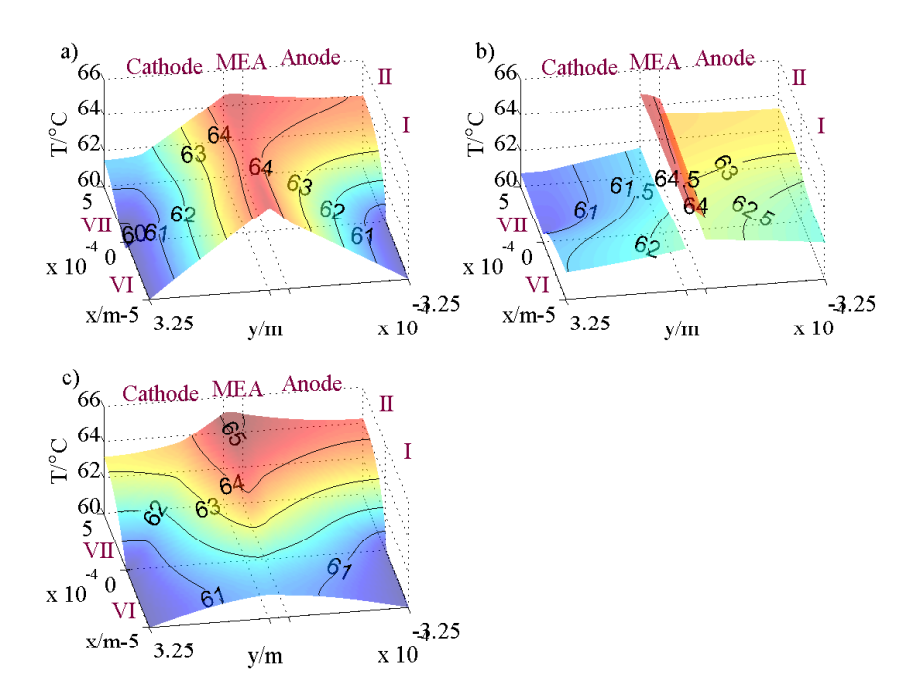


Figure 4.5. Temperature distributions ($E^{\text{cell}} = 0.6 \text{ V}$): a) effective thermal conductivity; b) thermal bulk and contact conductivities; c) alternative capillary pressure expression.

The fourth and last PEFC model (Paper 4) is similar to the two-phase model outlined above, with the difference that it considers a net-type flow field for the cell. An expression for the current density of the cathode was found from parameter adaption to an iR-corrected polarization curve, obtained with a segmented cell, as shown in Figure 4.6. The model is able to predict the iR-corrected behavior, the measured cell potential for the whole cell as well as the resulting power density.

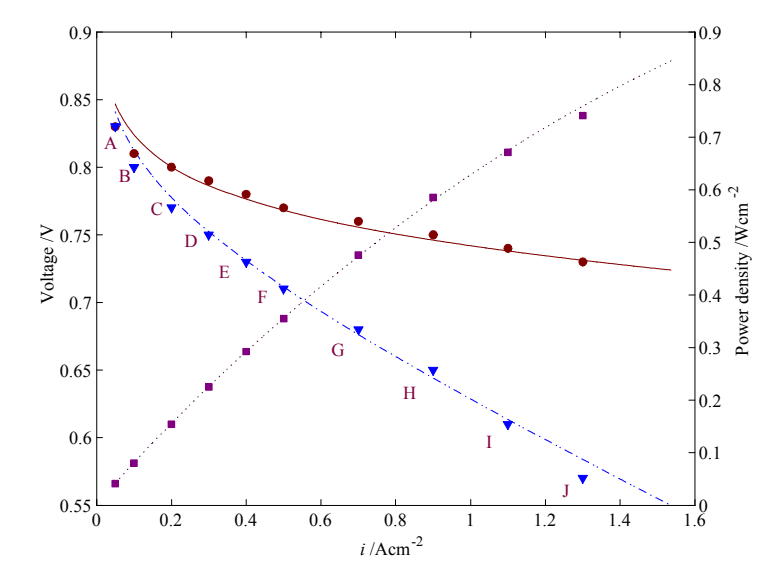


Figure 4.6. Polarization curve: (\blacktriangledown) is the measured potential of the segmented cell; (\bullet) is the iR-corrected potential of the segmented cell; (\blacksquare) is the power density of the segmented cell; (--) is the predicted potential of the model; (--) is the predicted power density of the model. The measurement points are denoted by A to J.

2. Direct methanol fuel cells

Two isothermal models that take conservation of mass, momentum and species in the anode have been derived and analyzed. The first (Paper 5) considers the liquid-phase for a flow field comprising a channel, and the second (Paper 7) is a two-phase mixture model, where the gas phase is accounted for and the flow channel exchanged for a net. The computational domain is similar to that of the cathode, as illustrated in Figure 4.1. The slenderness of the anode allows a considerable reduction of the mathematical formulations, without sacrificing any of the essential physics. From the modelling point of view, an important advantage of the reduced approach, based on nondimensionalization and elementary asymptotic techniques, is that it leads to an understanding of the important transport mechanisms for momentum, mass and species that would have been difficult to discern from simply a numerical solution of the full set of equations. Both reduced models are then verified and the two-phase model validated against experimental data obtained with a visual cell.

For the liquid phase model, we found that the flow in the anode can be described by three dimensionless parameters, $\Delta, \Omega, \mathcal{H}$, given in terms of operating, design and physical parameters. In addition, differences and similarities between different types of fuel cells become apparent. For instance, in contrast to the cathode of a PEFC, where the flow induced by the electrochemical reaction at the catalytic layer was found to have a leading order effect on the flow field in the channel (Paper 1), the velocity induced by the electrochemical reaction in the anode of the DMFC has a negligible effect on the channel flow field, which leads to a decoupling of the momentum equations and furthermore allows us to write the velocity field in the channel in closed form. In addition, although the equations of the reduced model must themselves be solved numerically, the computational cost is considerably smaller than that incurred when using commercial software to solve the full set. This can be of benefit both for thorough parameter studies, as well as for system studies of DMFCs.

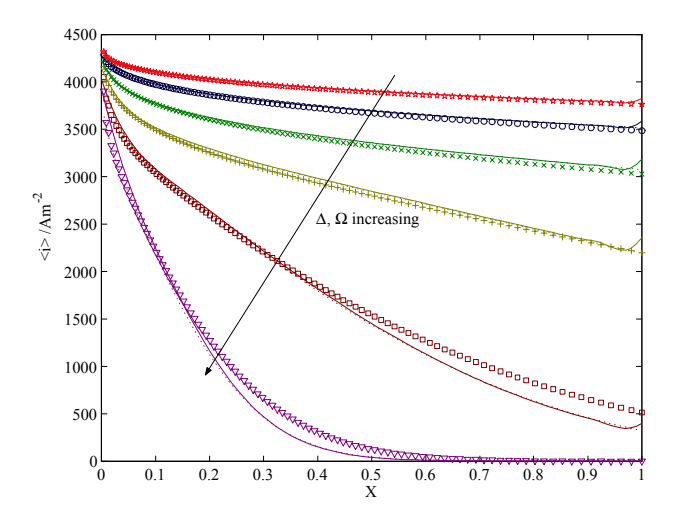


Figure 4.7. Verification of the reduced model. (\cdots) corresponds to the CFX-4.4 solution with 10^4 number of nodes, (-) is the Femlab solution for ~ 1000 adapted nodes and markers are for the reduced model, with 10^4 cells. (\bigstar) : $\Delta = 0.932$, (o): $\Delta = 2.79$, (\times) : $\Delta = 9.32$, (+): $\Delta = 27.9$, (\square) : $\Delta = 93.2$, (∇) : $\Delta = 279$.

From the point of view of predicting fuel cell performance, a parameter study has shown that the current density distribution is far from even, especially for higher values of Δ , i.e. lower inlet velocities or longer anodes, as shown in Figure 4.7. We also found that performance can be improved by choosing thin porous backings (small \mathcal{H}) and running the cell at smaller values of Δ : these will reduce the mass transfer limitations in the porous backing and the flow channel, respectively.

The mass fraction of the carbon dioxide in the liquid phase leads to high supersaturations, whence carbon dioxide will vaporize for all operationally realistic values of Δ and evolve as a gas. To capture this gas phase, a multiphase mixture model was chosen, where we account for both the liquid and gas flow in the anode.

After verification, the model was validated against experiments with a visual cell (Paper 6). This cell, equipped with a transparent end plate at the anode, gave valuable information in terms of pressure drops, gas saturations and polarization curves at different temperatures.

From an analysis, the Ca, Gr, Gl and Sc numbers appear in addition to Δ , Ω and \mathcal{H} , which emerged from the analysis of the liquid phase model.

The pressure drop increases significantly when a current is drawn, as shown in Figure 4.8.

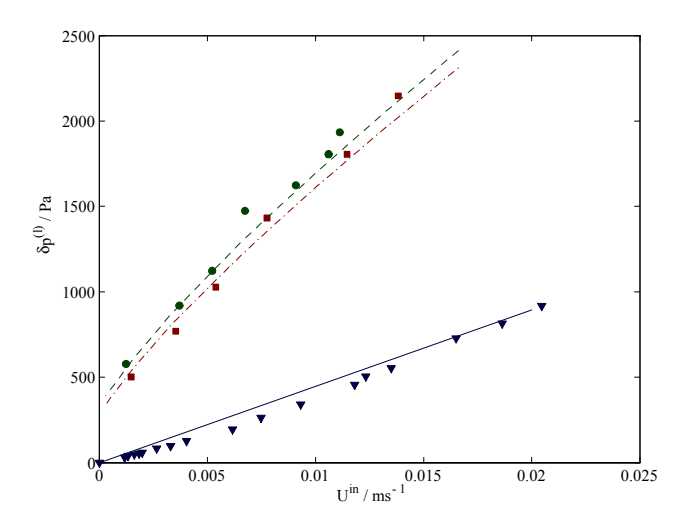


Figure 4.8. Pressure drops $\delta p^{(1)} = p^{(1)}(x=0) - p^{(1)}(x=L)$ from experiments and predictions from the reduced model. Experimental values: (\blacktriangledown) no current, (\blacksquare) 68 mA cm⁻² and (\bullet) 79 mA cm⁻². Model predictions: (—) no current, ($-\cdot$) 68 mA cm⁻², and ($-\cdot$) 79 mA cm⁻². The temperature is 45°C.

The reason for this drastic increase is the high gas saturation in the mesh, measured with the visual cell to be typically $\gtrsim 70\%$. This sharp increase in the gas saturation occurs close to the inlet, after which the increase is more moderate, as depicted in Figure 4.9. The presence of the gas phase was found to improve the mass transfer of methanol, especially at higher temperatures, when the mole fraction of methanol in the gas phase is also higher.

Furthermore, it was demonstrated that at low temperatures (≤30°C), a liquid-phase model can be sufficient for predicting the anode performance, which allows for a considerable reduction in computational cost.

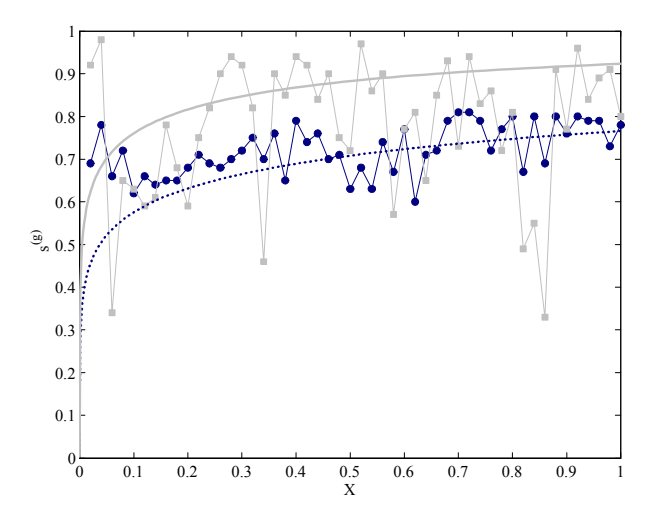


Figure 4.9. Gas saturation profiles in the streamwise direction according to experiments and model predictions at 45°C and 68 mA cm⁻². Experimental values: (\blacksquare) 1.4×10^{-3} m s⁻¹, and (\bullet) 1.3×10^{-2} m s⁻¹. Model predictions: (--) 1.4×10^{-3} m s⁻¹, and (\cdots) 1.3×10^{-2} m s⁻¹.

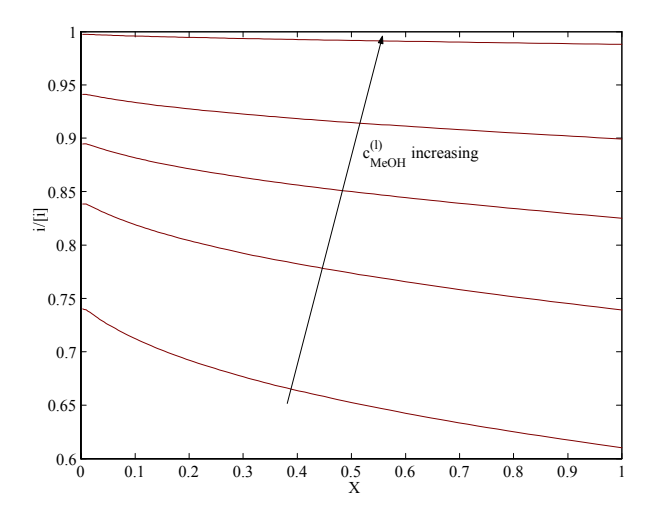


Figure 4.10. The local current density along the streamwise axis at 50°C, and $U^{\rm in}=7.3\times10^{-3}~{\rm m~s^{-1}}$. The concentrations of methanol are: 0.10, 0.50, 1.0, 2.0 and 4.0 M.

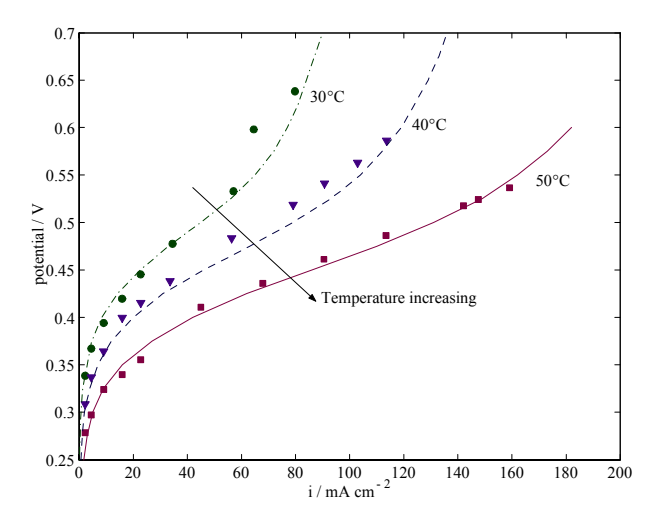


Figure 4.11. Polarization curves for experiments and model predictions. The inlet velocity $U^{\rm in} = 7.3 \times 10^{-3} \ {\rm m \ s^{-1}}$ and the methanol concentration is 1 M. Experimental values: (•) 30°C , (▼) 40°C, and (■) 50°C. Model predictions: (- ·-) 30°C, (--) 40°C and (—) 50°C.

From Figure 4.10, we discern that for the highest concentration of methanol studied, 4 M, the local current density stays close to the current density scale [i], based on the inlet methanol concentration. At such high methanol concentrations, the anode model can be reduced to just computing [i], which entails virtually no computational cost.

Polarization curves at 30°C, 40°C and 50°C were measured and as can be inferred from Figure 4.11, the model predictions follow the measured curves well. An increase in temperature is mirrored by an increase in cell performance, as the oxidation kinetics are faster and the gas phase contains more methanol at higher temperatures.

The observations from the flow visualization and model, suggest the characteristics of an 'ideal' flow field for the anode of a DMFC: the flow field should retain the bubbles to keep the gas saturation high, whilst ensuring that the entrapped gas remains in contact with "fresh" liquid fuel flowing past the entrapped bubbles.

CHAPTER 5

Discussion and Outlook

Several models have been derived for the polymer electrolyte and direct methanol fuel cell in an effort to capture the essential physics, so as to ascertain the main transport mechanisms and parameters as well as predict the main features: mass transfer limitations; cell performance; thermal and water management (PEFC); gas management (DMFC). In tandem with and prior to numerical treatments, nondimensionalization, scaling arguments and elementary asymptotic techniques have provided valuable insight and allowed for considerable reductions of the governing set of equations, alleviating computational complexity and cost.

Experiments with a segmented cell (PEFC) and a visual cell (DMFC) have allowed for parameter adaption where necessary and validation of the predictive capabilities of several of the models (Paper 4 and 7). Throughout the work, focus has been on the most limiting half cells: the cathode of the PEFC; the anode for the DMFC.

The first model (Paper 1), considering gas phase flow for a slender cathode (PEFC), showed that the cathode performance can be conveniently summarized in a novel and compact way by polarization surfaces, which take into account geometrical, hydrodynamical and electrochemical features. This model provides a good framework for inclusion and subsequent study of two-phase flow and thermal effects in the cathode.

An extension (Paper 2) to allow for a fully three dimensional cathode predicted that the interdigitated flow channel design can sustain the highest currents, compared to parallel channels in co- and counterflow and a foam, if channeling effects can be avoided. As for paper 1, more physics should be added to the model, followed by validation with the segmented cell, preferably equipped with different flow fields, to guarantee that the model predictions are accurate.

Upon introducing the liquid phase in addition to the gas phase, the dimensionality was reduced to two dimensions, taking a flow field comprising parallel channels (Paper 3) and a net (Paper 4) into account. The electrokinetics of the cathode were found from parameter adaption to polarization curves from a segmented cell, equipped with a net-type flow field. The two-phase model was found to predict the cell performance accurately, both in terms of iR-corrected and cell voltages. Adding a more detailed membrane model and resolving the anode in terms of conservation of mass, species and momentum would yield

a complete PEFC model for a cross-section, where effects such as membrane dehydration could be studied.

The two models (Paper 5 and 7) derived for the anode of a DMFC, exploited the slenderness, similar to the first model for the PEFC (Paper 1), and lead to reduced models, where the momentum equations were shown to decouple from the mass and species equations, and closed form solutions could be secured a priori to any computations. Verification against the full set of equations ensured that the reduced models are valid within the limits imposed by the operational and geometrical parameters of the anode. Furthermore, pressure drops, gas saturation distributions in the anode and polarization curves for varying temperatures, allowed for parameter adaption and subsequent validation (Paper 7). The presence of a gas phase was shown to facilitate the cell performance, especially so at higher temperatures, due to the increased methanol content in the gas. The impact of the gas phase on the anode of the DMFC should be studied further, both in terms of modeling and experiments. For this purpose, the visual cell (Paper 6) could be equipped with flow fields of varying gas permeability and, if possible, be segmented to obtain information on the local current density distributions.

The models that have been derived and analyzed in this thesis focus on the limiting half cells. While these are crucial to cell performance, the membrane and opposite electrode are still important. Inclusion of membrane models, preferably parameter adapted and validated, as well as the opposite electrode would yield models that can predict the cell performance completely. Subsequent analysis should allow for reductions of the governing equations, similar to the ones obtained here.

Furthermore, the dynamic behavior of the fuel cells has not been touched upon in this thesis, and represents an interesting extension for future work.

The segmented cell is a powerful tool for acquiring experimental information about the current densities, both on a local and global level, thus providing invaluable information for cell design and model development, and should be further employed.

Perhaps most importantly though, is the determination of physical parameters of the various components of the cell, such as capillary pressures, relative permeabilites and thermal contact conductivities. At present, there is a serious need to quantify these.

Acknowledgments

First of all, I would like to thank my supervisor Michael Vynnycky for his invaluable advice during the years and for introducing me to scaling and asymptotic analysis. I am going to miss our discussions.

From the depths of my heart to Kah Wai Lum: thank you for coming to the conference in the Netherlands that destiny-laden year, and for the deepening relationship ever since.

The cooperation with Joakim Nordlund and Matti Noponen has been inspiring and fruitful, for which I am very grateful.

I would also like to thank Göran Lindbergh and Fritz Bark for their support and advice and Jari Ihonen and Frédéric Jaouen for many discussions on the more practical aspects of fuel cells.

A special thanks goes to the undergraduate students that have been part of the ongoing fuel cell research at FaxénLaboratoriet and the Department of Applied Electrochemistry, KTH: H. Ekström, C. Picard and A. Björnsdotter Abrams.

To all the undergraduate students that I have had the joy and privilege to teach the basic an continuation courses in mechanics: it has been a pleasure to try to teach you the concepts of mechanics, to go strolling in the woods with you and to see you pass the courses with a smile on your faces.

I also wish to thank my colleagues, friends and room mates at the Department of Mechanics for providing a very stimulating atmosphere and many a shared meal.

The financial support from the Swedish Foundation for Strategic Environmental Research, MISTRA, and from the Swedish National Energy Administration is gratefully acknowledged. The work was done within the framework of the Jungner Center.

Finally, I dedicate this thesis to my parents, without whom I would not be where I am today.

Bibliography

- [1] U. Bossel, The Birth of the Fuel Cell 1835-1845, European Fuel Cell Forum, (2000).
- [2] J. Larminie and A. Dicks, Fuel Cell Systems Explained, John Wiley & Sons, (2002).
- [3] F. Jaouen, G. Lindbergh and G. Sundholm, J. Electrochem. Soc., 149, A437 (2002).
- [4] D. M. BERNARDI AND M. W. VERBRUGGE, AIChE Journal, 37, 1151 (1991).
- D. M. Bernardi and M. W. Verbrugge, J. Electrochem. Soc., 139, 2477 (1992).
- [6] T. E. Springer, T. A. Zawodzinski and S. Gottesfeld, J. Electrochem. Soc., 138, 2334 (1991).
- [7] V. Gurau, F. Barbir and H. Liu, J. Electrochem. Soc., 147, 2468 (2000).
- [8] K. DANNENBERG, P. EKDUNGE AND G. LINDBERGH, Journal of Applied Electrochemistry, 30, 1377 (2000).
- [9] T. F. Fuller and J. Newman, J. Electrochem. Soc., 140, 1218 (1993).
- [10] T. V. NGUYEN AND R. E. WHITE, J. Electrochem. Soc., 140, 2178 (1993).
- [11] J. S. YI AND T. V. NGUYEN, J. Electrochem. Soc., 145, 1149 (1998).
- [12] A. KAZIM, H. T. LIU AND P. FORGES, Journal of Applied Electrochemistry, 29, 1409 (1999).
- [13] J. S. YI AND T. V. NGUYEN, J. Electrochem. Soc., 146, 38 (1999).
- [14] K. W. Lum, Three Dimensional Computational Modelling of a Polymer Electrolyte Fuel Cell, Ph.D. dissertation, University of Loughborough (2003).
- [15] P. Futerko and I-M. Hsing, Electrochimica Acta, 45, 1741 (2000).
- [16] V. Gurau, H. Liu and S. Kakac, AIChE Journal, 44, 2410 (1998).
- [17] I-M. HSING AND P. FUTERKO, Chemical Engineering Science, 55, 4209 (2000).
- [18] D. Singh, D. M. Lu and N. Djilali, International Journal of Engineering Science, 37, 431 (1999).
- [19] S. Dutta, S. Shimpalee and J. W. van Zee, *J. Appl. Electrochem.*, **30**, 135 (2000).
- [20] S. DUTTA, S. SHIMPALEE AND J. W. VAN ZEE, Int. J. Heat and Mass Transfer, 44, 2029 (2001).
- [21] S. Shimpalee and S. Dutta, Numerical Heat Transfer, 38, Part A, 111 (2000).
- [22] P. Costamagna, Chem. Eng. Science, 56, 323 (2001).
- [23] W. HE, J. S. YI AND T. V. NGUYEN, AICHE J., 10, 2053 (2000)
- [24] D. NATARAJAN AND T.V. NGUYEN, J. Electrochem. Soc., 148, A1324 (2001).
- [25] L.B. Wang, Nobuko I. Wakayama and Tatsuhiro Okada, Electrochemistry Communications, 4, 584 (2002).
- [26] L. You and H. Liu, Int. J. Heat Mass Transfer, 45, 2277 (2002).
- [27] Z.H. WANG, C.Y. WANG AND K.S. CHEN, Journal of Power Sources, 94, 40 (2001).
- [28] N. DJILALI AND D. LU, Int. J. Therm. Sci., 41, 29 (2002).
- [29] G. J. M. Janssen, J. Electrochem. Soc., 148, A1313 (2001).
- [30] M. Wöhr, K. Bolwin, W. Schnurnberger, M. Fischer, W. Neubrand and G. Eigenberger, Int. J. Hydrogen Energy, 23, 213 (1998).
- [31] T. Berning and N. Djilali, J. Electrochem. Soc., 150, A1598 (2003).
- [32] S. MAZUMDER AND J. V. COLE, J. Electrochem. Soc., 150,A1510 (2003).
- [33] E. BIRGERSSON, J. NORDLUND, H. EKSTRÖM, M. VYNNYCKY, G. LINDBERGH, J. Electrochem. Soc., 150, A1368 (2003).

- [34] K. Scott, W. Taama and J. Cruickshank, J. Power Sources, 65, 159 (1997).
- [35] K. Scott, W. Taama and J. Cruickshank, J. Appl. Electrochem., 28, 289 (1998).
- [36] S.F. Baxter, V.S. Battaglia and R.E. White, J. Electrochem. Soc., 146, 437 (1999).
- [37] A.A. Kulikovsky, J. Divisek and A.A. Kornyshev, J. Electrochem. Soc., 147, 953 (2000).
- [38] H. Dohle, J. Divisek and R. Jung, J. Power Sources, 86, 469 (2000).
- [39] K. Scott, P. Argyropoulos and K. Sundmacher, J. Electroanal. Chem., 477, 97 (1999).
- [40] A.A. Kulikovsky, J. Appl. Electrochem., 30, 1005 (2000).
- [41] P.S. Kauranen, Acta Polytechnica Scandinavica, 237, 1 (1996).
- [42] K. SUNDMACHER, T. SCHULTZ, S. ZHOU, K. SCOTT, M. GINKEL AND E.D. GILLES, Chem. Eng. Sci., 56, 333 (2001).
- [43] S. ZHOU, T. SCHULTZ, M. PEGLOW AND K. SUNDMACHER, Phys. Chem. Chem. Phys., 3, 347 (2001).
- [44] A.A. Kulikovsky, Electrochem. Comm., 3, 460 (2001).
- [45] A.A. Kulikovsky, Electrochem. Comm., 3, 572 (2001).
- [46] J. NORDLUND, G. LINDBERGH, J. Electrochem. Soc., 149, A1107 (2002).
- [47] J.P. MEYERS, J. NEWMAN, J. Electrochem. Soc., 149, A710 (2002).
- [48] J.P. MEYERS, J. NEWMAN, J. Electrochem. Soc., 149, A718 (2002).
- [49] J.P. MEYERS, J. NEWMAN, J. Electrochem. Soc., 149, A729 (2002).
- [50] Z.H. WANG AND C.Y. WANG, Proceedings volume 2001-4, The Electroch. Soc., USA, p. 286 (2001).
- [51] J. DIVISEK, J. FUHRMANN, K. GÄRTNER AND R. JUNG, J. Electrochem. Soc., 150, A811 (2003).
- [52] C.Y. WANG AND P. CHENG, Int. J. Heat Mass Transfer, 39, 3607 (1996).
- [53] J. IHONEN, F. JAOUEN, G. LINDBERGH, A. LUNDBLAD AND G. SUNDHOLM, J. Electrochem. Soc., 149, A448 (2002).
- [54] W. HE, J. S. YI AND T. V. NGUYEN, AICHE Journal, 46, 2053 (2000).
- [55] J. NORDLUND AND G. LINDBERGH, J. Electrochem. Soc., 149, A1107 (2002).
- [56] J. Nordlund and G. Lindbergh, submitted to J. Electrochem. Soc.
- [57] T. CEBECI AND P. BRADSHAW, Momentum Transfer in Boundary Layers, Washington: Hemisphere Publishing Corporation (1977).
- [58] Matlab, http://www.mathworks.com/.
- [59] J. C. TANNEHILL, D. A. ANDERSON AND R. H. PLETCHER, Computational Fluid Mechanics and Heat Transfer, 2nd ed., p 462, Taylor & Francis, USA (1997).
- [60] FEMLAB 2.3, http://www.comsol.se.
- [61] CFX-4.4, http://www.cfx.aeat.com.
- [62] MAPLE 7, http://www.maplesoft.com/.
- [63] J. IHONEN, Development of Characterisation Methods for the Components of the Polymer Electrolyte Fuel Cell, Ph.D. dissertation, KTH, Sweden (2003).